PAPER

Check for updates

Highly efficient ethanol vapour detection using g-C₃N₄/ZnO micro flower-like heterostructural composites†

Xianfeng Zhang, [ID] Wenjie Du, Qian Li and Changpeng Lv [ID] *

This work proposes precursor pyrolysis, ultrasonic exfoliation and hydrothermal methods as well as high-temperature calcination strategies to fabricate heterostructured g-C₃N₄/ZnO composites with excellent ethanol vapour sensing properties. The structure, composition and morphology of the as-prepared g-C₃N₄/ZnO composites were characterized using X-ray diffraction (XRD), X-ray photoelectron spectroscopy (XPS), field-emission scanning electron microscopy (SEM), transmission electron microscopy (TEM) and Fourier transform infrared spectroscopy (FTIR). Then, the sensing properties of the g-C₃N₄/ZnO composites for ethanol (C_2H_5OH) were studied, and g-C₃N₄ doping with different mass ratios was used to control the gas-sensing properties of the composites. Compared with pure ZnO and g-C₃N₄, the performance of g-C₃N₄ with 1% doping content is the best, and the gas sensing activity of the 1% g-C₃N₄/ZnO composite is greatly improved at the optimal working temperature (280 °C). The response to 100 ppm ethanol reaches 81.4, which is 3.7 times that of the pure ZnO-based sensor under the same conditions. In addition, the sensor has good selectivity as well as fast response and recovery speeds (24 s and 63 s, respectively). Finally, a reasonable gas sensing enhancement mechanism is proposed, and it is believed that the constructed g-C₃N₄/ZnO micro flower-like heterostructure and the distinct positions of the valence and conduction bands of ZnO and g-C₃N₄ lead to the obtained sensor exhibiting a large specific surface area and increased conductivity, thereby improving the g-C₃N₄/ZnO-based sensor sensing performance.

1. Introduction

In recent years, semiconductor metal oxide gas sensors have played an important role in environmental monitoring, chemical reaction process control, and personal safety due to their low cost, simple fabrication, and wide detection range.[1–5] In order to detect toxic and harmful pollutants in the environment in real time and avoid the threat to human health, scientists have researched nanomaterials with different structures, expecting to obtain gas sensors with industrial application value.[6,7] The excellent gas sensing performance verifies that these semiconductor oxide nanocomposites are a promising candidate for the gas sensor industry, for example, SnO₂/g-C₃N₄,[8] In₂O₃@GO,[9] Co₃O₄/ZnO,[10] *etc.* Zinc oxide (ZnO) is a wide-bandgap ($E = 3.3$ eV) N-type metal-oxide-semiconductor material that is widely used in the field of gas sensors due to its good chemical stability and low resistivity.[11–13] Cao *et al.* synthesized Pt-loaded ZnO nanosheets by a facile one-pot hydrothermal

route, the obtained 0.5% Pt/ZnO based gas sensor exhibited a response value of 3.57 for 50 ppm CO.[14] Shingange *et al.* composited ZnO and gold nanoparticles by the microwave method and tested the gas-sensing properties of the composite material.[15] The results showed that it had high response and selectivity to NH₃. Yan *et al.* prepared ZnO nanoparticle-encapsulated MoS₂ nanosheets by a two-step hydrothermal method, and the composite exhibited excellent gas-sensing properties to ethanol, which may have potential applications in ethanol vapour detection.[16] Although ZnO gas sensors have been well researched and applied, there are still many shortcomings. For example, the disadvantages of a high working temperature and poor selectivity still need continuous improvement.[17] Fortunately, the excellent thermal stability of g-C₃N₄ with a similar structure to graphene makes it promising as an additive to enhance the sensing performance at relatively high operating temperatures.[18] In addition, g-C₃N₄ is an indirect band gap semiconductor material with a moderate band gap (band gap width of 2.7 eV), which can be coupled with a variety of semiconductors, improve the separation efficiency of electrons and holes, and facilitate the transfer of electrons, helping to regulate the electrical properties of the semiconductor material to which it is coupled.[19] In addition, it also possesses a high specific surface area, good catalytic

Anhui Provincial Engineering Laboratory of Silicon-based Materials, School of Material and Chemical Engineering, Bengbu University, Bengbu 233030, People's Republic of China. E-mail: lvcp1213@gmail.com

performance and important 2D material properties.[20] By compounding g-C_3N_4 and ZnO, a gas sensor composed of zinc oxide nanomaterials and g-C_3N_4 is prepared, which realizes the integration of materials and functions and exerts the advantages of the two materials, which is of great significance for improving the sensing performance of materials. Finally, monolayer or multilayer g-C_3N_4 can be easily prepared by ultrasonically exfoliating bulk g-C_3N_4, which favours the formation of hierarchical structure composites between g-C_3N_4 nanosheets and ZnO.[21,22]

In order to improve the sensing performance of gas sensors, a series of metal oxide gas sensors with high specific surface area, high porosity and hollow internal nanostructures have been assembled, which are considered as candidates with strong potential for industrial applications. Zhan *et al.* developed gas sensor based on spherical porous SnO_2/ZIF-8 nanocomposite. The sensor has excellent sensing sensitivity, fast response and recovery time, and good selectivity.[23] Hussain *et al.* successfully prepared polyhedron CeO_2 for formaldehyde gas-sensing applications. The enhancement of the sensor response was attributed to the multifaceted polyhedral nanostructures.[24] Wang *et al.* synthesized 2D/2D ZnO/g-C_3N_4 heterojunction composites by ultrasonic mixing and subsequent calcination. The gas-sensing properties of visible light/ultraviolet LED light source activation to NO_2 were investigated at room temperature. When the ZnO/g-C_3N_4 composite was illuminated at 460 nm, it showed the highest response of 44.8 for 7 ppm NO_2, and the response time and recovery time were 142 s and 190 s, respectively.[25] Qin *et al.* prepared CuO–ZnO/g-C_3N_4 ternary composite by one-step hydrothermal method, the as-prepared composite exhibited obviously enhanced sensing performance to ethanol.[26] Cao *et al.* reported the synthesis of cocoon-like ZnO-decorated g-C_3N_4 hybrid nanocomposites by a hydrothermal method using PEG400 as a surfactant.[27] The gas sensing properties of the as-prepared g-C_3N_4/ZnO nanocomposites were investigated. However, the g-C_3N_4/ZnO-based sensor prepared by this method has a high working temperature (350 °C), the response is not too high, and the response to 100 ppm ethanol is only 15.8.

Herein, heterostructural g-C_3N_4/ZnO nanocomposites were prepared for efficient ethanol vapour detection. First, single-layer or multilayer g-C_3N_4 was prepared by high-temperature calcination and ultrasonic exfoliation, and then heterostructural g-C_3N_4/ZnO micro flower-like composites were prepared by a hydrothermal method (Scheme 1). The microstructure, morphology, chemical state and surface structure of the samples were investigated by XRD, XPS, SEM, TEM and FTIR. The g-C_3N_4 nanosheets further enhance the sensing

performance of ZnO. A comprehensive study of the sensor's working temperature, response, sensitivity, selectivity, and stability was carried out using a gas-sensing test system. The response value and response/recovery time were analysed by the response recovery characteristic curve to determine whether the hierarchical nanostructure exhibited better sensing performance and the optimal g-C_3N_4 doping amount. Finally, the gas sensing mechanism of g-C_3N_4/ZnO nanocomposites is discussed.

2. Experimental

2.1 Chemicals

Melamine and urea were purchased from the Shanghai Macklin Biochemical Technology Co., Ltd. Anhydrous ethanol and zinc acetate were acquired from the Sinopharm Chemical Reagent Co., Ltd., and all of the reagents used in the experiment were of analytical grade.

### 2.2 Preparation of g-C_3N_4 nanosheets

Five grams of melamine was placed in an alumina crucible, heated from room temperature to 550 °C at a heating rate of 5 °C min^{-1} in a muffle furnace, and kept for 5 h. After cooling to room temperature naturally, the samples were ground in a mortar. Then, the samples were washed with anhydrous ethanol and ultrasonicated for 2 h, the supernatant was removed and centrifuged, the product was collected, and the washing was repeated 3 times. Finally, the samples were dried in a drying oven at 50 °C for 2 h to remove ethanol and water to obtain a dry light yellow powder, namely, g-C_3N_4 nanosheets, which were stored for subsequent use.

2.3 Preparation of g-C_3N_4/ZnO composites

An appropriate amount of g-C_3N_4 powder (0.0025 g, 0.0049 g, 0.0099 g) was weighed and dispersed in 10 mL of deionized water and stirred with a glass rod to form a suspension. A total of 1.3170 g of zinc acetate was weighed and dissolved in 20 mL of deionized water with stirring, poured into the above g-C_3N_4 suspension, stirred and mixed evenly, and sonicated for 30 min. The suspension was poured into 30 mL of 0.4 mol L^{-1} urea solution, mixed evenly, poured into the reaction kettle, and reacted at 120 °C for 10 h. After natural cooling, the lower precipitate was removed and washed three times with deionized water. The product was collected by centrifugation and dried in a drying oven at 60 °C for 12 h. Finally, the product was calcined at 400 °C for 2 h at a heating rate of 5 °C min^{-1} in a muffle furnace to obtain g-C_3N_4/ZnO composites with different g-C_3N_4 contents, which are marked as x% g-C_3N_4/ZnO for simplicity, where x represents the weight percent of g-C_3N_4 in the composite. For comparison, the exact same procedure was also used to synthesize pure ZnO without the addition of g-C_3N_4 nanosheets.

2.4 Characterization

The crystal structure of the samples was characterized by X-ray diffraction (Rigaku SmartLab SE, Japan) under the following
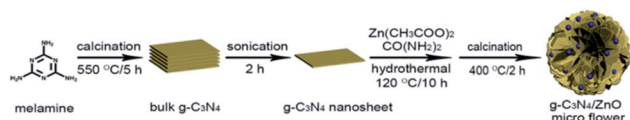
Scheme 1 Schematic illustration of the facile synthesis of g-C_3N_4/ZnO micro flower-like composite.

operating conditions: copper target, scanning voltage of 30 kV, current of 40 mA, and scanning angle of 10°–80°. Fourier transformed infrared (FTIR) spectra of the samples were tested in the range of 400–4000 cm^{-1} with a resolution of 1 cm^{-1} using an infrared spectrometer (Thermo Fisher Nicolet iS10, USA). Transmission electron microscopy (TEM) images were obtained by transmission electron microscopy (Hitachi JEM-2010, Japan) at 200 kV by depositing g-C$_3$N$_4$, ZnO and g-C$_3$N$_4$/ZnO dispersions in ethanol onto a 400-mesh carbon-coated copper grid and letting the solvent dry to prepare samples for analysis. Field emission scanning electron microscopy (SEM) images (Hitachi S-4800, Japan) were used to characterize the microscopic morphology of the samples. Thermogravimetric analysis (TGA) was recorded on a thermogravimetric analyser (Netzsch STA2500 Regulus, Germany) in dry air, and the sample was heated from room temperature to 500 °C at a rate of 10 °C min^{-1}. Nitrogen adsorption and desorption curves were measured by an accelerated surface area porosimetry system (Micromeritics ASAP 2020, USA), and the Brunauer–Emmett–Teller (BET) equation was used to calculate the specific surface areas of the samples from their adsorption data. X-ray photoelectron spectroscopy (XPS) was performed using an ESCALAB 250Xi (Thermo Fisher Scientific, USA) instrument and multiple surface analysis techniques.

2.5 Preparation and gas sensing performance test of the side-heating gas sensing component

Approximately 0.05 g of the powder was taken and ground in a mortar, and then 100 μL of deionized water was added for mixing and grinding to obtain a paste-like slurry. The paste was evenly scribbled on the surface of the Al$_2$O$_3$ ceramic tube, and the ceramic tube was dried in an oven at 80 °C for 5 h to completely remove moisture. The nichrome wire ($R = 28$ ohm) was inserted into the ceramic tube to control the heating temperature, and 4 platinum wires and 2 nichrome wires were welded from the ceramic tube to the hexagonal base. To increase the stability and repeatability of the gas sensor components, the soldered components were placed on an ageing table for 3 days at 300 °C. Finally, the required side-heating gas sensor was obtained for gas-sensing testing (Fig. S1†). The gas-sensing properties of the material were determined on a gas-sensing component test system (Zhengzhou Weisheng WS-30A, Fig. S2†), and the test was performed using the static gas distribution method. The sensor response is defined as $S = R_a/R_g$, where R_a and R_g refer to the resistance value of the gas-sensitive material in air and the resistance value of the measured gas at a certain working temperature, respectively.[28–30] All gas-sensing property testing experiments were performed at room temperature (25 ± 2 °C), and the relative humidity (RH) was maintained at (50 ± 5)% RH.

3. Results and discussion

3.1 Characterization of samples

The crystal structure and surface functional groups of the samples were analysed by XRD and FTIR, respectively. The constituent elements and chemical bonds of the composites were analysed by XPS, and the structure and morphology of the samples were observed by TEM and SEM.

As shown in Fig. 1a, the diffraction peak at $2\theta = 27.36°$ in the XRD spectrum of the pure g-C$_3$N$_4$ sample corresponds to the (002) crystal plane of g-C$_3$N$_4$ (JCPDS no. 87-1526); this can be attributed to the interlayer stacking of aromatic compounds and is consistent with literature reports.[31] The XRD patterns of pure ZnO and g-C$_3$N$_4$/ZnO with different mass ratios were shown in Fig. 1a, it can be observed that there are obvious diffraction peaks corresponding to the (100), (002), (101), (102) (110), (103), (200), (112), and (201) crystal planes of hexagonal wurtzite ZnO (JCPDS no. 36-1451). However, after doping with g-C$_3$N$_4$, the characteristic peak of g-C$_3$N$_4$ does not appear in the spectrum, even if the XRD patterns of g-C$_3$N$_4$ and 2% g-C$_3$N$_4$/ZnO composites were displayed in logarithmic scale, the doped g-C$_3$N$_4$ impurity phase was not observed (Fig. S3†), which may be caused by the low content of g-C$_3$N$_4$. The characteristic peak intensity of 2% g-C$_3$N$_4$/ZnO in the spectrum is obviously smaller than that of the pure ZnO sample, indicating that the growth of ZnO crystals is affected by g-C$_3$N$_4$, and the greater the doping, the more obvious the intensity decrease.

Fig. 1b shows the full scan XPS spectra of the g-C$_3$N$_4$/ZnO composite. According to the positions of the characteristic peaks in the spectrum, the sample can be qualitatively analysed to determine the constituent elements and chemical bonds of the composite material. Fig. 1b shows that the composite material is composed of four elements: C, N, Zn, and O. The figure shows that the six peaks at 86.92 eV, 285.80 eV, 398.47 eV, 529.80 eV, 1021.58 eV, and 1044.25 eV are assigned to Zn 3p, C 1s, N 1s, O 1s, Zn 2p$_{3/2}$ and Zn 2p$_{1/2}$, respectively.[32] The three peaks shown in Fig. 1c are 284.8 eV, 286.4 eV and 287.6 eV, corresponding to the C–N–C and C=N, N–C=N structures, respectively.[33] The peak at 398.45 eV in Fig. 1d corresponds to the formation of C=N–C.[34,35] From Lorentz–Gaussian fitting of the O 1s spectrum in Fig. 1e, it is known that there are three intense subpeaks centered at 529.9 (OI), 531.1 (OII), and 532.8 eV (OIII). The three peaks are assigned to O^{2-} ions in the ZnO crystal lattice, the oxygen species at the surface oxygen-deficient regions of ZnO and weakly bonded hydroxyl species absorbed on the surface, respectively.[36–38] The two characteristic peaks at 1021.29 eV and 1044.46 eV in Fig. 1f indicate the existence of ZnO in the form of Zn^{2+}, which is consistent with the literature reports.[39] XPS spectrum analysis shows that the obtained sample is a g-C$_3$N$_4$/ZnO composite material.

Fig. 2 shows the FTIR spectra of g-C$_3$N$_4$, ZnO and g-C$_3$N$_4$/ZnO samples doped with different mass ratios. For the FTIR spectrum of pure g-C$_3$N$_4$, there is an absorption peak at 810 cm^{-1} related to the bending vibration of the triazine ring of the g-C$_3$N$_4$ unit structure, and the absorption peaks at 1230, 1462, 1560 and 1640 cm^{-1} are attributed to the g-C$_3$N$_4$ heterocyclic ring caused by the stretching vibration of C–N.[40] The peak at 3200 cm^{-1} is attributed to the stretching vibration of NH$_2$ or NH groups on the defect site of the aromatic ring terminal in g-C$_3$N$_4$.[41] For the pure ZnO sample, the absorption peak at 432 cm^{-1} is assigned to the stretching vibration of Zn–O in ZnO. By comparing the FTIR spectra of g-C$_3$N$_4$, ZnO and g-C$_3$N$_4$/ZnO,
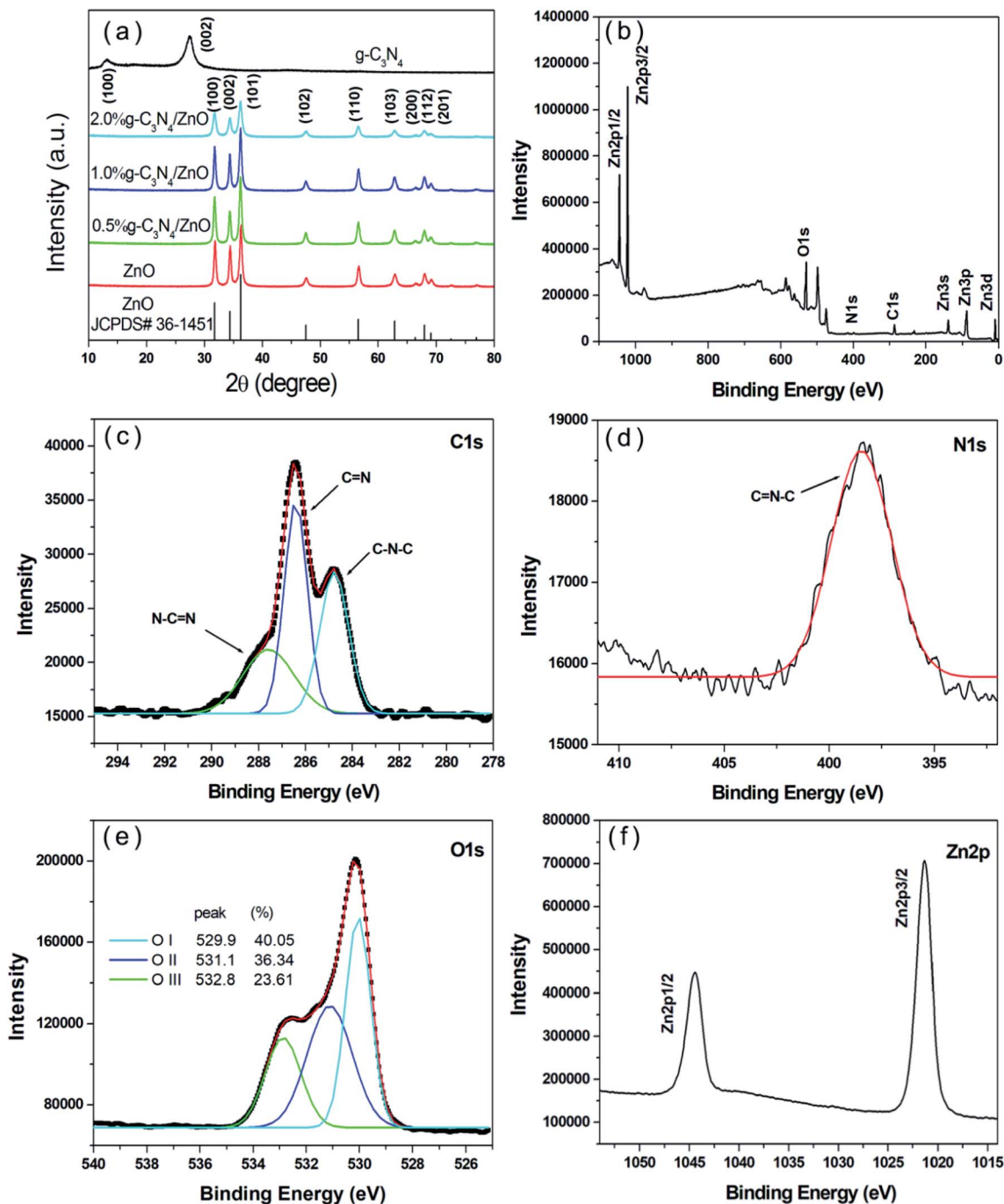
Fig. 1 (a) XRD patterns of the samples and (b) the full range XPS, (c) C 1s, (d) N 1s, (e) O 1s, and (f) Zn 2p spectra of the 1% g-C$_3$N$_4$/ZnO composite.

the doped ZnO has a characteristic absorption peak of C–N vibration, indicating that the sample was successfully doped with g-C$_3$N$_4$. In addition, it can be seen from the FTIR spectra that the g-C$_3$N$_4$/ZnO composite has some deviations in some peaks compared with pure g-C$_3$N$_4$ and ZnO. The stretching vibration peak of Zn–O is shifted from 432 to 445 cm^{-1}, the stretching vibration absorption peak of C–N is shifted from 810 to 846 cm^{-1}, and the stretching vibration peak of N–H is shifted from 3200 to 3445 cm^{-1}. This shows that the mixed effect of ZnO and g-C$_3$N$_4$ changes the framework structure, and at the

same time, the chemical bond between ZnO and g-C$_3$N$_4$ interacts.[42]

The morphology and microstructure of nanomaterials have an important influence on their macroscopic properties, and special microstructures generally exhibit special properties. The morphology and structure of the prepared samples were characterized by SEM and TEM. The as-prepared g-C$_3$N$_4$ exhibits a two-dimensional sheet-like structure (Fig. 3a), and the pure ZnO shows a spherical structure with a particle size of approximately 50–150 nm (Fig. 3b). Fig. 3c shows the SEM picture of
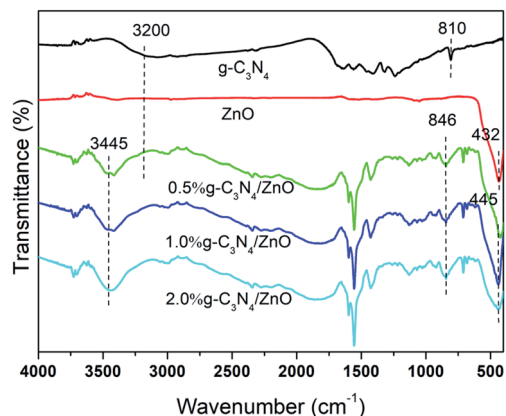
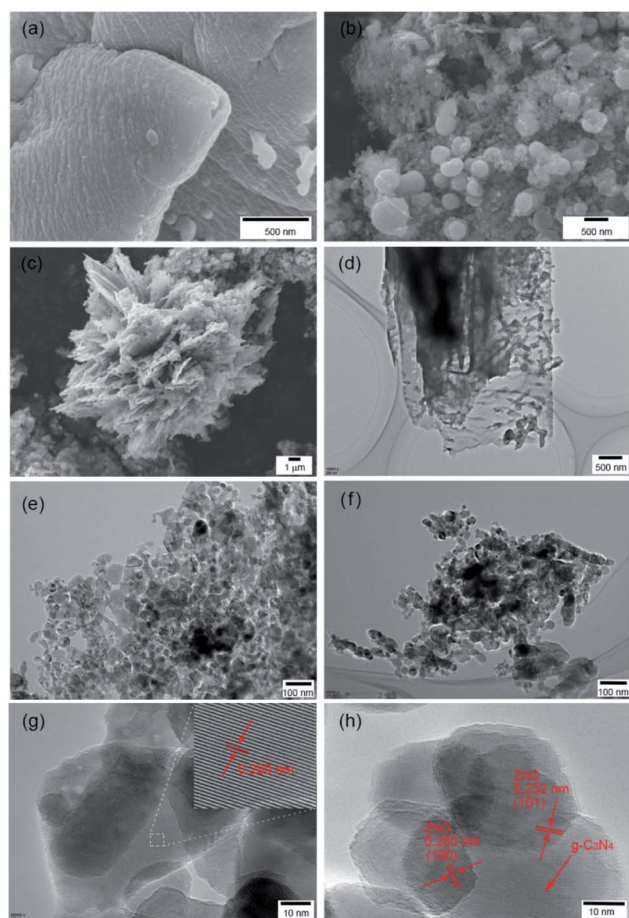**Fig. 2** FTIR spectra of the obtained g-C$_3$N$_4$, ZnO and g-C$_3$N$_4$/ZnO composites.

Fig. 3 SEM images of (a) g-C$_3$N$_4$, (b) ZnO, and (c) 1% g-C$_3$N$_4$/ZnO composite, and TEM images of (d) g-C$_3$N$_4$, (e) ZnO, and (f) 1% g-C$_3$N$_4$/ZnO composite, and high-resolution images of (g) ZnO and (h) 1% g-C$_3$N$_4$/ZnO composite.

the hybridized g-C$_3$N$_4$/ZnO nanocomposite. It can be clearly observed that a large number of ZnO nanoparticles are anchored on the C$_3$N$_4$ layer to form a three-dimensional micro flower heterostructure (Fig. 3c). The microstructures of g-C$_3$N$_4$,

ZnO, and g-C$_3$N$_4$/ZnO samples were further observed by TEM. It can be seen from Fig. 3d that g-C$_3$N$_4$ is a transparent ultrathin nanosheet, and pure ZnO appears as quasispherical nanoparticles (Fig. 3e). When Zn(CH$_3$COO)$_2$, urea and g-C$_3$N$_4$ underwent a high-temperature and high-pressure hydrothermal reaction together, large amount of ZnO nanoparticles were deposited and anchored on the g-C$_3$N$_4$ layer, and further calcination was performed to remove impurities such as small organic molecules, and finally heterostructures were constructed between g-C$_3$N$_4$ and ZnO. The TEM image of the composite shows that there are obvious ZnO aggregated particles on g-C$_3$N$_4$ (Fig. 3f). From the high-resolution TEM images in Fig. 3g and h, the interplanar distances of 0.280 nm and 0.252 nm correspond to the (100) and (101) planes for the ZnO hexagonal wurtzite phase, respectively. Meanwhile, the high-resolution images of g-C$_3$N$_4$/ZnO composites clearly reveal the heterojunction interface between g-C$_3$N$_4$ nanosheets and ZnO nanoparticles. Both SEM and TEM images indicate that ZnO nanoparticles can be directly anchored on the C$_3$N$_4$ layer to form a heterostructured C$_3$N$_4$/ZnO during the simple hydrothermal process.

3.2 Performance test of the gas sensor

First, the sensor response of the prepared gas-sensing material to 100 ppm ethanol at different working temperatures was investigated. Fig. S4† shows the response of pure ZnO as well as those of g-C$_3$N$_4$/ZnO composites with different g-C$_3$N$_4$ contents to 100 ppm ethanol at different operating temperatures (240 °C to 400 °C). It is clear from the figure that the responses to ethanol varied with temperature, and all curves exhibited an "increase-maximum-decrease" trend. This is consistent with literature reports.[42] At low temperature, the activation energy of ethanol molecules was not enough to react with oxygen species adsorbed on the surface, resulting in a low response. With increasing temperature, the reactivity of adsorbed oxygen on the surface of the gas-sensing material increases, and the conversion of surface-adsorbed oxygen species helps to improve the sensor response. After reaching the optimal working temperature, further increasing the temperature causes a decrease in the adsorption capacity of ethanol molecules, resulting in a decrease in the response of the sensing material. This behaviour can be due to the thermodynamics and kinetics of gas adsorption and desorption on the surface of gas sensitive material. The maximum responses for ZnO, 0.5% g-C$_3$N$_4$/ZnO, 1% g-C$_3$N$_4$/ZnO, and 2% g-C$_3$N$_4$/ZnO samples appeared at 340 °C, 300 °C, 280 °C and 360 °C, respectively. This result suggests that the combination of an appropriate amount of g-C$_3$N$_4$ can significantly reduce the optimal gas sensing working temperature of ZnO. The response is the highest for the 1% g-C$_3$N$_4$/ZnO sample; therefore, 280 °C was determined to be the optimal working temperature for further study. The thermal stability of g-C$_3$N$_4$/ZnO composite was further confirmed by TGA. Fig. S5† shows the thermogravimetric curve of the obtained g-C$_3$N$_4$/ZnO composite. When the temperature is heated to 500 °C, almost no weight loss is observed, which is consistent with previous literature reports,[43] which also indicates that g-

C_3N_4/ZnO gas sensing materials present good thermal stability in the working temperature range.

At an operating temperature of 280 °C, it can be seen from the response of ZnO gas sensors with different g-C_3N_4 doping amounts to 100 ppm ethanol that the response also increases with increasing g-C_3N_4 doping amount (Fig. S6†). When the content of g-C_3N_4 is 1%, its response is the highest, and then it decreases rapidly. Doping a certain amount of g-C_3N_4 has the ability to increase the electron conduction rate, thus improving the gas sensing performance, but g-C_3N_4 has a high resistance value, and excessive doping will lead to the resistance of the composite material being too high, reducing the electron conduction rate. From the R_a values of ZnO and g-C_3N_4/ZnO composites at different operating temperatures, it can be seen that the resistance value of the composites doped with g-C_3N_4 is significantly higher than that of pure ZnO at the same operating temperature in the range of 240–340 °C. It is noteworthy that the change of resistance value of g-C_3N_4/ZnO with temperature is more obvious than that of pure ZnO (Table S1†).

Humidity is one of the important challenges for the reliability and stability of chemiresistive sensors, because it affects their electrical properties and will lead to poor sensing response to the target gas. For comparison, the g-C_3N_4/ZnO sensor was tested toward 250 ppm ethanol vapor in the presence of relative humidity. The RH range is between 40 and 50% with an interval of 10%. It is clearly observed that when the g-C_3N_4/ZnO sensor is exposed to ethanol vapor, the sensor showed a change in resistance (Fig. S7a†). When the RH increased from 40% to 60%, the response value increased from 72.6 to 154.8 (Fig. S7b†). This indicated that the material is prone to water vapour when reacting with adsorbed oxygen and releasing electrons, which leads to an increase in sensor's response.[44]

The dynamic resistance curve is also a key parameter for evaluating sensor performance, as it reflects real-time response for the sensors. Fig. 4a shows the typical resistance-recovery characteristics of a 1% g-C_3N_4/ZnO-based sensor to different concentrations of ethanol vapour. It can be clearly seen that the resistance of the sensor decreases with increasing ethanol concentration, and the response values for 2, 5, 10, 25, 50, 75, 100, 200, and 500 ppm ethanol vapour are 1.51, 3.46, 9.01, 26.36, 48.17, 69.43, 81.4, 96.56, and 131.48 (Table S2†), respectively. This may be because the reaction between the gas and the adsorbed oxygen on the surface of the material is continuously enhanced with the gradual increase in the ethanol concentration, and the response value of ethanol increases rapidly. It then rapidly returned to baseline as the ethanol was depleted in the closed test chamber, showing that the gas sensor exhibited excellent response behavior and was fully reversible over a wide range of ethanol concentrations. To clarify the ethanol-sensing activity, Fig. S8† shows the sensing responses of ZnO, g-C_3N_4, and g-C_3N_4/ZnO composite to different concentration ethanol. The pure g-C_3N_4 nanosheets are nonsensitive to ethanol, implying that ethanol-sensing comes from ZnO. For pure ZnO, it is not very sensitive to ethanol, showing a poor ethanol sensing response, which is 1, 1.5, 2.9, 5.1, 8.2, 15, 22, 28.2, 35.1, corresponding to 2, 5, 10, 25, 50, 75, 100, 200, 500 ppm ethanol vapour, respectively. When ZnO was modified with 1% g-C_3N_4,

the composite showed much higher ethanol sensing activity than pure ZnO under the condition of tested ethanol concentration, and the response value of 1% g-C_3N_4/ZnO composite to 100 ppm ethanol is 3.7 times that of pure ZnO. These results suggest that the modification of g-C_3N_4 nanosheets is beneficial for the ethanol sensing performance of the ZnO sensor. A good linear relationship between response value and the ethanol concentration was exhibited in the range of 2–100 ppm ($S = 1.75 + 0.8504c$[ethanol]; $R = 0.9935$) (Fig. 4b), according to the sensitivity can be computed as the slope of the linear fit on the curve,[44] the sensor displayed a sensitivity value of 0.850 ppm^{-1} toward ethanol. In addition, the limit of detection (LOD) was calculated according to the formula LOD $= 3 \times$ (rms$_{noise}$/slope),[44,45] where rms$_{noise}$ denotes root-mean-square (rms) deviation of the baseline before the exposure to ethanol vapour. The calculated LOD was 244 ppb, indicating that the detection limit of the prepared gas sensing component is lower. After the ethanol concentration exceeds 100 ppm, with the further increase of the gas concentration, the increase rate of the gas sensing response value slows down, and the gas sensing response follows another linear relationship from 100 to 500 ppm. The reason may be that the higher gas concentration will cause the gas-sensing material adsorption to be saturated and the conductance response to be distorted from the original linearity.[46] The response time of the gas sensor is defined as the time from contacting the gas to be tested to reaching 90% of the steady state, and the recovery time is the time from the beginning of contact with the air to the time of 90% of the steady state.[47] The measured response and recovery times to 100 ppm ethanol vapour were 24 seconds and 63 seconds, respectively (Fig. S9†).

Selectivity is an important parameter of gas sensors and is the ability of the sensor to respond to a certain gas in the presence of different gases. Fig. 4c shows the response of the 1% g-C_3N_4/ZnO gas sensor to 100 ppm methanol, ethanol, isopropanol, n-butanol, toluene, formic acid, and ammonia at the working temperature of 280 °C, corresponding to 8.2, 81.4, 25.5, 17.5, 12, 9.5 and 7.5. It is evident that the sensor based on the 1% g-C_3N_4/ZnO nanocomposite exhibits high sensitivity and selectivity towards ethanol. The good selectivity of the obtained material to ethanol may be because ethanol is more active to lose electrons during the redox reaction with absorbed oxygen, and the hydroxyl group (–OH) is more easily oxidized at the optimal working temperature.[26] This indicates that the g-C_3N_4/ZnO complex has a high potential application value in the preparation of low-concentration ethanol detectors.

Long-term stability and repeatability are also the important parameters for gas sensors. Fig. 4d shows the response of the 1% g-C_3N_4/ZnO composite to 60 ppm ethanol vapour for 30 days at the optimal operating temperature. Within 30 days, the baseline resistance of the sensor is relatively stable but decreases slightly, the response of the composite to 60 ppm ethanol decreased from 52.85 to 45.76 (Fig. S10 and Table S3†). The response value decreased by 13.42% after 30 days. Therefore, the response value of the sensor is relatively stable, but the long-term stability needs to be further improved in order to make it more applicable. The repeatability of the proposed
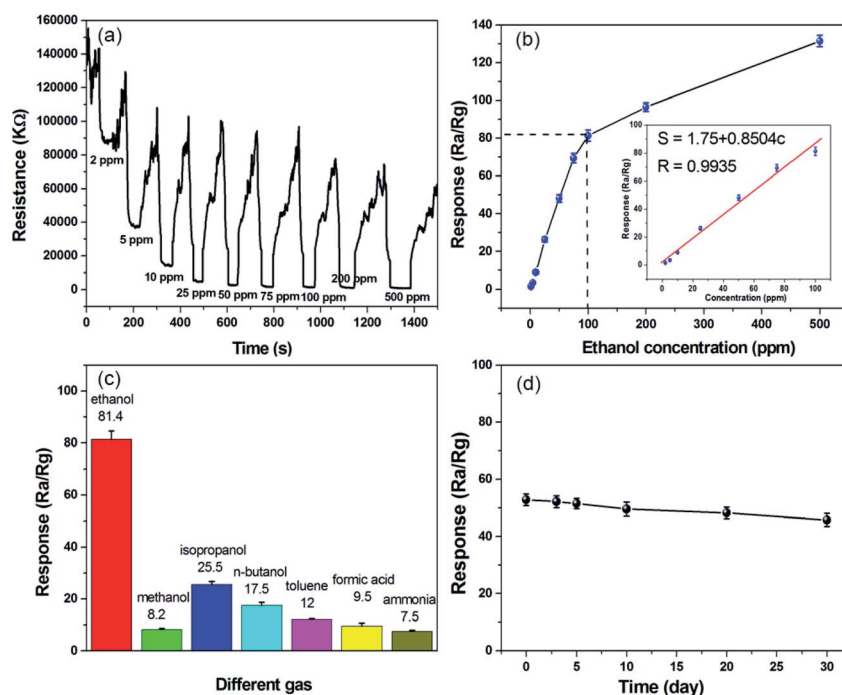
Fig. 4 (a) The dynamic resistance curve of the 1% g-C$_3$N$_4$/ZnO composite to different ethanol concentrations (2–500 ppm) at the optimum working temperature. (b) The corresponding response value as a function of ethanol concentration. (c) Response of the 1% g-C$_3$N$_4$/ZnO gas sensor to different gases. (d) Response of 1% g-C$_3$N$_4$/ZnO composites to 60 ppm ethanol vapour as a function of time.

sensor is shown in Fig. S11.† After three consecutive tests, the response value of g-C$_3$N$_4$/ZnO basically remained at around 48. It possess excellent repeatability, indicating that the g-C$_3$N$_4$/ZnO based sensor could be used for ethanol gas sensor.

The sensing performance of ethanol sensors based on different materials is listed in Table S4.† The response values of 3D SnO$_2$ nanoflower, Au/3D SnO$_2$ microstructure, RGO/hollow SnO$_2$, Pt/3D SnO$_2$ nanoflower, SnO$_2$/g-C$_3$N$_4$ and cocoon-like ZnO/g-C$_3$N$_4$ are 7, 30, 70.4, 8, 105, and 15.8, respectively. In this work, the response value of 1% g-C$_3$N$_4$/ZnO micro flower-like heterostructural composites to 100 ppm ethanol was 81.4 at 280 °C. Therefore, C$_3$N$_4$/ZnO composites possess good ethanol sensing performance, which exhibit a great potential application in the field of gas sensors.

3.3 Proposed gas sensing mechanism

The widely accepted gas-sensing mechanism for semiconductor oxide sensors is based on the change in sensor resistance caused by the adsorption and desorption of gas molecules and chemical reactions on the surface of the sensing material.[48,49] ZnO is a well-known surface resistance-controlled gas sensor material. When a g-C$_3$N$_4$/ZnO nanomaterial based gas sensor is placed in the air, the gas sensor will adsorb O$_2$ in the air. Under certain temperature conditions, these oxygen atoms will obtain electrons from the conduction band of ZnO materials and exist on the surface of ZnO-sensitive materials in the form of ions (O$_2^-$, O$^-$, and O^{2-}),[34] and form a depletion layer at the ZnO nanostructures interface. Meanwhile, the coupling effect of the heterostructure possibly occurs due to the special positions of

the valence and conduction bands between ZnO and g-C$_3$N$_4$,[19,32,44] which causes the electrons migrate to the heterostructure surface until the Fermi levels of the two materials are aligned. During this process, the free electron concentration in ZnO decreases, resulting in a wider depletion layer and increased resistance. When the g-C$_3$N$_4$/ZnO based gas sensor is placed in ethanol gas, the ethanol gas will react with the oxygen ions on the surface of the ZnO sensitive material as follows:

$$C_2H_5OH + 6O^-(ads) \rightarrow 3H_2O + 2CO_2 + 6e^-$$
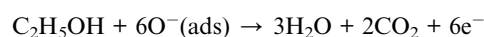
The electrons generated by this reaction return to the ZnO material (Fig. 5), leading to the increase of electron concentration of ZnO, therefore, the surface depletion layer of ZnO could be easily modified by the electrons from oxygen species. This reflects the significant decrease in the resistance of the g-C$_3$N$_4$/ZnO sensor. Therefore, when the sensor switches from air to ethanol vapour, a greater resistance change can be obtained, and a higher response can be obtained accordingly. Furthermore, the addition of g-C$_3$N$_4$ leads to the formation of nanostructures with higher specific surface area. The specific surface area is 23.25 m^2 g^{-1}, which is higher than that of pure ZnO$_2$ (9.14 m^2 g^{-1}) (Fig. S12†). This is very conducive to the adsorption and diffusion of ethanol and oxygen molecules. Moreover, the introduction of g-C$_3$N$_4$ enhanced the conductivity to facilitate the detection of resistance changes.[50] In a word, the three-dimensional intercalated structure g-C$_3$N$_4$/ZnO micro flower material prepared in this work exhibits a large specific surface
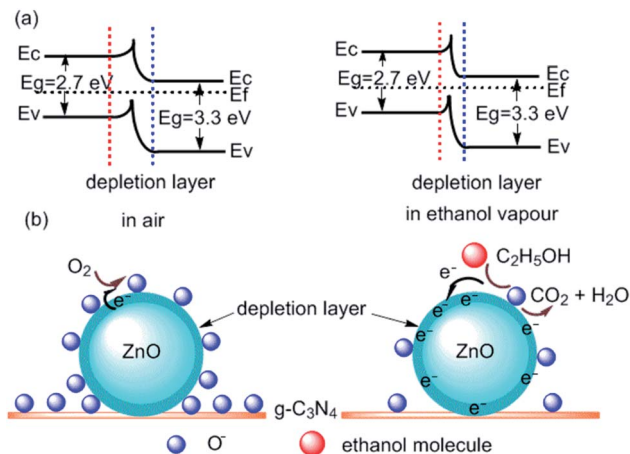
Fig. 5 (a) Bandgap diagram of g-C$_3$N$_4$/ZnO nanocomposites; (b) schematic diagram of ethanol sensing mechanism of g-C$_3$N$_4$/ZnO nanocomposites in air and ethanol vapour.

area and increased conductivity, this may be the reason why the sensing performance of the gas sensor is significantly enhanced. We will make much more efforts to verify the gas sensing mechanism.

4. Conclusions

In summary, single-layer or multilayer g-C$_3$N$_4$ was prepared by ultrasonic exfoliation of bulk g-C$_3$N$_4$, and then the heterostructural composites with micro flower-like structures were successfully prepared by combining the hydrothermal method and high-temperature calcination strategy. Compared with the gas-sensing properties of pure ZnO, the gas-sensing properties of the prepared 1% g-C$_3$N$_4$/ZnO composites showed that doping a certain amount of g-C$_3$N$_4$ could improve the detection sensitivity of ZnO for ethanol, and the response was increased by 3.7 times. It has good selectivity as well as fast response and recovery speeds (24 seconds and 63 seconds). In addition, a reasonable gas sensing enhancement mechanism is proposed, the prepared g-C$_3$N$_4$/ZnO material has a micro flower-like heterostructure with a larger specific surface area, which improves its ability to adsorb more O$_2$ and C$_2$H$_5$OH molecules, and it is believed that the introduction of g-C$_3$N$_4$ enhanced the conductivity to facilitate the detection of resistance changes. As a result, the sensing performance of the gas sensor is significantly improved.

Conflicts of interest

There are no conflicts to declare.

Acknowledgements

References

1 Y. H. Li, W. Luo, N. Qin, J. P. Dong, J. Wei, W. Li, S. S. Feng, J. C. Chen, J. Q. Xu, A. A. Elzatahry, M. H. Es-Saheb, Y. H. Deng and D. Y. Zhao, Highly ordered mesoporous tungsten oxides with a large pore size and crystalline framework for H$_2$S sensing, *Angew. Chem., Int. Ed.*, 2014, **53**(34), 9035–9040.

2 J. Zhang, Z. Y. Qin, D. W. Zeng and C. S. Xie, Metal-oxide-semiconductor based gas sensors: screening, preparation, and integration, *Phys. Chem. Chem. Phys.*, 2017, **19**, 6313–6329.

3 D. David, W. Udo and B. Nicolae, Current understanding of the fundamental mechanisms of doped and loaded semiconducting metal oxide-based gas sensing materials, *ACS Sens.*, 2019, **4**, 2228–2249.

4 N. Rahman, J. Yang, Zulfiqar, M. Sohail, R. Khan, A. Iqbal, C. Maouche, A. A. Khan, M. Husain, S. A. Khattak, S. N. Khan and A. Khan, Insight into metallic oxide semiconductor (SnO$_2$, ZnO, CuO, α-Fe$_2$O$_3$, WO$_3$)-carbon nitride (g-C$_3$N$_4$) heterojunction for gas sensing application, *Sens. Actuators, A*, 2021, **332**, 113128.

5 B. Mondal and P. K. Gogoi, Nanoscale heterostructured materials based on metal oxides for a chemiresistive gas sensor, *ACS Appl. Electron. Mater.*, 2022, **4**(1), 59–86.

6 S. Hussain, X. Y. Yang, M. K. Aslam, A. Shaheen, M. S. Javed, N. Aslam, B. Aslam, G. W. Liu and G. J. Qiao, Robust TiN nanoparticles polysulfide anchor for Li–S storage and diffusion pathways using first principle calculations, *Chem. Eng. J.*, 2020, **391**, 123595.

7 S. Hussain, M. S. Javed, S. Asim, A. Shaheen, A. J. Khan, Y. Abbas, N. Ullah, A. Iqbal, M. S. Wang, G. J. Qiao and S. Yun, Novel gravel-like NiMoO$_4$ nanoparticles on carbon cloth for outstanding supercapacitor applications, *Ceram. Int.*, 2020, **46**(5), 6406–6412.

8 J. L. Cao, C. Qin and Y. Wang, Synthesis of g-C$_3$N$_4$ nanosheets decorated flower-like tin oxide composites and their improved ethanol gas sensing properties, *J. Alloys Compd.*, 2017, **728**, 1101–1109.

9 S. Shah, S. Han, S. Hussain, G. W. Liu, T. F. Shi, A. Shaheen, Z. W. Xu, M. S. Wang and G. J. Qiao, NO$_2$ gas sensing responses of In$_2$O$_3$ nanoparticles decorated on GO nanosheets, *Ceram. Int.*, 2022, **48**, 12291–12298.

10 T. F. Shi, H. G. Hou, S. Hussain, C. X. Ge, M. A. Alsaiari, A. S. Alkorbi, G. W. Liu, R. Alsaiari and G. J. Qiao, Efficient detection of hazardous H$_2$S gas using multifaceted Co$_3$O$_4$/ZnO hollow nanostructures, *Chemosphere*, 2022, **287**, 132171.

11 S. Kanaparthi and S. G. Singh, Chemiresistive sensor based on zinc oxide nanoflakes for CO$_2$ detection, *ACS Appl. Nano Mater.*, 2019, **2**(2), 700–706.

12 J.-W. Kim, Y. Porte, K. Y. Ko, H. Kim and J.-M. Myoung, Micropatternable double-faced ZnO nanoflowers for

flexible gas sensor, *ACS Appl. Mater. Interfaces*, 2017, **9**(38), 32876–32886.

13 J. Y. Xuan, G. D. Zhao, M. L. Sun, F. C. Jia, X. M. Wang, T. Zhou, G. C. Yin and B. Liu, Low-temperature operating ZnO-based NO_2 sensors: a review, *RSC Adv.*, 2020, **10**, 39786–39807.

14 Y. Wang, X. N. Meng and J. L. Cao, Rapid detection of low concentration CO using Pt-loaded ZnO nanosheets, *J. Hazard. Mater.*, 2020, **381**, 120944.

15 K. Shingange, Z. P. Tshabalala, O. M. Ntwaeaborwa, D. E. Motaung and G. H. Mhlongo, Highly selective NH_3 gas sensor based on Au loaded ZnO nanostructures prepared using microwave-assisted method, *J. Colloid Interface Sci.*, 2016, **479**, 127–138.

16 H. Yan, P. Song, S. Zhang, Z. Yang and Q. Wang, Facile synthesis, characterization and gas sensing performance of ZnO nanoparticles-coated MoS_2 nanosheets, *J. Alloys Compd.*, 2016, **662**, 118–125.

17 C. C. Hsiao and L. S. Luo, A rapid process for fabricating gas sensors, *Sensors*, 2014, **14**, 12219–12232.

18 W. Lu, T. Xu, Y. Wang, H. Hu, N. Li, X. Jiang and W. Chen, Synergistic photocatalytic properties and mechanism of g-C_3N_4 coupled with zinc phthalocyanine catalyst under visible light irradiation, *Appl. Catal., B*, 2016, **180**, 20–28.

19 J. Wen, J. Xie, X. Chen and X. Li, A review on g-C_3N_4-based photocatalysts, *Appl. Surf. Sci.*, 2017, **391**, 72–123.

20 S. P. S. David, S. Veeralakshmi, S. Nehru and S. Kalaiselvam, A highly sensitive, selective and room temperature operatable formaldehyde gas sensor using chemiresistive g-C_3N_4/ZnO, *Mater. Adv.*, 2020, **1**, 2781–2788.

21 M. Yongning, L. Enzhou, H. Xiaoyun, T. Chunni, W. Jun, L. Juan and F. Jun, A simple process to prepare few-layer g-C_3N_4 nanosheets with enhanced photocatalytic activities, *Appl. Surf. Sci.*, 2015, **358**, 246–251.

22 D. Wang, S. M. Huang, H. J. Li, A. Y. Chen, P. Wang, J. Yang, X. Y. Wang and J. H. Yang, Ultrathin WO_3 nanosheets modified by g-C_3N_4 for highly efficient acetone vapor detection, *Sens. Actuators, B*, 2019, **282**, 961–971.

23 M. M. Zhan, C. X. Ge, S. Hussain, A. S. Alkorbi, R. Alsaiari, N. A. Alhemiary, G. J. Qiao and G. W. Liu, Enhanced NO_2 gas-sensing performance by core-shell SnO_2/ZIF-8 nanospheres, *Chemosphere*, 2022, **291**, 132842.

24 S. Hussain, N. Aslam, X. Yang, M. S. Javeed, Z. W. Xu, M. S. Wang, G. W. Liu and G. J. Qiao, Unique polyhedron CeO_2 nanostructures for superior formaldehyde gas-sensing performances, *Ceram. Int.*, 2018, **44**, 19624–19630.

25 H. T. Wang, J. H. Bai, M. Dai, K. P. Liu, Y. Y. Liu, L. S. Zhou, F. M. Liu, F. M. Liu, Y. Gao, X. Yan and G. Y. Lu, Visible light activated excellent NO_2 sensing based on 2D/2D ZnO/g-C_3N_4 heterojunction composites, *Sens. Actuators, B*, 2020, **304**, 127287.

26 C. Qin, Y. Wang, Y. X. Gong, Z. Y. Zhang and J. L. Cao, CuO-ZnO hetero-junctions decorated graphitic carbon nitride hybrid nanocomposite: hydrothermal synthesis and ethanol gas sensing application, *J. Alloys Compd.*, 2019, **770**, 972–980.

27 J. Cao, Y. Gong, Y. Wang, B. Zhang, H. Zhang, G. Sun, H. Bala and Z. Zhang, Cocoon-like ZnO decorated graphitic carbon nitride nanocomposite: hydrothermal synthesis and ethanol gas sensing application, *Mater. Lett.*, 2017, **198**, 76–80.

28 W. W. Guo, Q. L. Zhou, J. Zhang, M. Fu, N. Radacsi and Y. X. Li, Hydrothermal synthesis of Bi-doped SnO_2/rGO nanocomposites and the enhanced gas sensing performance to benzene, *Sens. Actuators, B*, 2019, **299**, 126959.

29 W. W. Guo, B. Y. Zhao, Q. L. Zhou, Y. Z. He, Z. C. Wang and N. Radacsi, Fe-doped ZnO/reduced graphene oxide nanocomposite with synergic enhanced gas sensing performance for the effective detection of formaldehyde, *ACS Omega*, 2019, **4**, 10252–10262.

30 V. S. Bhati, M. Kumar and R. Banerjee, Gas sensing performance of 2D nanomaterials/metal oxide nanocomposites: a review, *J. Mater. Chem. C*, 2021, **9**, 8776–8808.

31 W. J. Zhang, C. H. Xu, E. Z. Liu, J. Fan and X. Y. Hu, Facile strategy to construction Z-scheme $ZnCo_2O_4$/g-C_3N_4 photocatalyst with efficient H_2 evolution activity, *Appl. Surf. Sci.*, 2020, **515**, 146039.

32 P. Fageria, R. Nazir, S. Gangopadhyay, H. C. Barshilia and S. Pande, Graphitic-carbon nitride support for the synthesis of shape-dependent ZnO and their application in visible light photocatalysts, *RSC Adv.*, 2015, **5**, 80397–80409.

33 J. Hu, C. Zou, Y. Su, M. Li, Z. Yang, M. Ge and Y. Zhang, One-step synthesis of 2D C_3N_4-tin oxide gas sensors for enhanced acetone vapor detection, *Sens. Actuators, B*, 2017, **253**, 641–651.

34 J. L. Zhai, T. Wang, C. Wang and D. C. Liu, UV-light-assisted ethanol sensing characteristics of g-C_3N_4/ZnO composites at room temperature, *Appl. Surf. Sci.*, 2018, **441**, 317–323.

35 Y. Zhang, J. S. Liu, X. F. Chu, S. M. Liang and L. Kong, Preparation of g–C_3N_4–SnO_2 composites for application as acetic acid sensor, *J. Alloys Compd.*, 2020, **832**, 153355.

36 X. G. Han, H. Z. He, Q. Kuang, X. Zhou, X. H. Zhang, T. Xu, Z. X. Xie and L. S. Zheng, Controlling morphologies and tuning the related properties of nano/microstructured ZnO crystallites, *J. Phys. Chem. C*, 2009, **113**, 584–589.

37 N. Han, X. F. Wu, L. Y. Chai, H. D. Liu and Y. F. Chen, Counterintuitive sensing mechanism of ZnO nanoparticle based gas sensors, *Sens. Actuators, B*, 2010, **150**, 230–238.

38 J. Guo, J. Zhang, M. Zhu, D. X. Ju, H. Y. Xu and B. Q. Cao, High-performance gas sensor based on ZnO nanowires functionalized by Au nanoparticles, *Sens. Actuators, B*, 2014, **199**, 339–345.

39 S. Kumar, A. Baruah, S. Tonda, B. Kumar, V. Shanker and B. Sreedhar, Cost-effective and eco-friendly synthesis of novel and stable N-doped ZnO/g-C_3N_4 core–shell nanoplates with excellent visible-light responsive photocatalysis, *Nanoscale*, 2014, **6**, 4830–4842.

40 P. He, L. Song, S. Zhang, X. Wu and Q. Wei, Synthesis of g-C_3N_4/Ag_3PO_4 heterojunction with enhanced photocatalytic performance, *Mater. Res. Bull.*, 2014, **51**, 432–437.

41 X. Yuan, S. Duan, G. Wu, L. Sun, G. Cao, D. Li, H. Xu, Q. Li and D. Xi, Enhanced catalytic ozonation performance of highly stabilized mesoporous ZnO doped g-C_3N_4 composite for efficient water decontamination, *Appl. Catal., A*, 2018, **551**, 129–138.

42 J. L. Cao, Y. X. Gong, Y. Wang, B. Zhang, H. L. Zhang, G. Sun, H. Bala and Z. Y. Zhang, Facile synthesis and high acetone gas sensing performances of popcorn-like In_2O_3 hierarchical nanostructures, *Mater. Lett.*, 2017, **186**, 256–258.

43 J.-X. Sun, Y.-P. Yuan, L.-G. Qiu, X. Jiang, A.-J. Xie, Y.-H. Shen and J.-F. Zhu, Fabrication of composite photocatalyst g-C_3N_4–ZnO and enhancement of photocatalytic activity under visible light, *Dalton Trans.*, 2012, **41**, 6756–6763.

44 Z. P. Tshabalala, T. P. Mokoena, M. Judalo, J. Tshikongo, T. K. Hillie, H. C. Swart and D. E. Motaung, TiO_2 nanowires for humidity-stable gas sensors for toluene and xylene, *ACS Appl. Nano Mater.*, 2021, **4**, 702–716.

45 T. P. Mokoena, H. C. Swart, K. T. Hillie and D. E. Motaung, Engineering of rare-earth Eu3+ ions doping on p-type NiO for selective detection of toluene gas sensing and luminescence properties, *Sens. Actuators, B*, 2021, **347**, 130530.

46 C. H. Zhao, W. Q. Hu, Z. X. Zhang, J. Y. Zhou, X. J. Pan and E. Q. Xie, Effects of SnO_2 additives on nanostructure and gas-sensing properties of α-Fe_2O_3 nanotubes, *Sens. Actuators, B*, 2014, **195**, 486–493.

47 W. W. Guo, L. L. Huang, J. Zhang, Y. Z. He and W. Zeng, Ni-doped SnO_2/g-C_3N_4 nanocomposite with enhanced gas sensing performance for the effective detection of acetone in diabetes diagnosis, *Sens. Actuators, B*, 2021, **334**, 129666.

48 R. Y. Miao, W. Zeng and Q. Gao, SDS-assisted hydrothermal synthesis of NiO flake-flower architectures with enhanced gas sensing properties, *Appl. Surf. Sci.*, 2016, **384**, 304–310.

49 L. Q. Sun, X. Han, K. Liu, S. Yin, Q. L. Chen, Q. Kuang, X. G. Han, Z. X. Xie and C. Wang, Template-free construction of hollow α-Fe_2O_3 hexagonal nanocolumn particles with an exposed special surface for advanced gas sensing properties, *Nanoscale*, 2015, **7**, 9416–9420.

50 Q. Lin, Y. Li and M. Yang, Tin oxide/graphene composite fabricated via a hydrothermal method for gas sensors working at room temperature, *Sens. Actuators, B*, 2012, **173**, 139–147.